Electrodynamic modeling of strong coupling between a metasurface and intersubband transitions in quantum wells

Salvatore Campione,[1,2,3,*] Alexander Benz,[2,3] John F. Klem,[2] Michael B. Sinclair,[2] Igal Brener,[2,3] and Filippo Capolino[1,*]

[1]*Department of Electrical Engineering and Computer Science, University of California Irvine, Irvine, California, 92697 USA*

[2]*Sandia National Laboratories, Albuquerque, New Mexico 87185 USA*

[3]*Center for Integrated Nanotechnologies (CINT), Sandia National Laboratories, Albuquerque, New Mexico 87185 USA*

(Received 2 November 2013; revised manuscript received 1 April 2014; published 28 April 2014)

Strong light-matter coupling has recently been demonstrated in subwavelength volumes by coupling engineered optical transitions in semiconductor heterostructures (e.g., quantum wells) to metasurface resonances via near fields. It has also been shown that different resonator shapes may lead to different Rabi splittings, though this has not yet been well explained. In this paper, our aim is to understand the correlation between resonator shape and Rabi splitting, in particular to determine and quantify the physical parameters that affect strong coupling by developing an equivalent circuit network model whose elements describe energy and dissipation. Because of the subwavelength dimension of each metasurface element, we resort to the quasistatic (electrostatic) description of the near field and hence define an equivalent capacitance associated to each dipolar element of a flat metasurface. We show that this is also able to accurately model the phenomenology involved in strong coupling between the metasurface and the intersubband transitions in quantum wells. We show that the spectral properties and stored energy of a metasurface/quantum-well system obtained using our model are in good agreement with both full-wave simulation and experimental results. We then analyze metasurfaces made of three resonator geometries and observe that the magnitude of the Rabi splitting increases with the resonator capacitance in agreement with our theory, providing a phenomenological explanation for the resonator shape dependence of the strong coupling process.

DOI: 10.1103/PhysRevB.89.165133 PACS number(s): 78.67.Pt, 41.20.Cv, 81.07.−b, 78.30.−j

I. INTRODUCTION

Metamaterials are artificial materials whose interaction with light results in interesting phenomena, including negative refraction [1,2], superresolution [3,4], artificial magnetism [5], and cloaking [6]. Recently, increasing emphasis has been placed on metasurfaces (MSs), i.e., single layers containing two-dimensional periodic sets of resonators, because their fabrication is compatible with standard semiconductor processing technology and is significantly simpler than that of three-dimensional (3D) metamaterials.

Metamaterials are able to localize intense electromagnetic fields in deep subwavelength volumes and thus are excellent candidates for the study of strong light-matter coupling—a process in which the excitation energy is periodically exchanged between matter (e.g., quantum wells, or QWs) and a MS (i.e., a cavity mode). When strong coupling is achieved, the following two properties are simultaneously observed: in the time domain, the electric field radiated by the cavity shows a beating mode at a characteristic time constant, and in the frequency domain, this beating corresponds to a splitting of the single bare cavity resonance into two polariton branches [7,8] with separation $2\Omega_R$, with Ω_R being the Rabi (angular) frequency.

The first experimental reports of strong coupling using intersubband transitions (ISTs) relied on the use of macroscopic optical cavities [9–16]. Recently, strong coupling has also been demonstrated through the use of a subwavelength metal-dielectric-metal microcavity [17] or MSs with subwavelength elements [18–21]. Strong light-matter interaction between planar MSs and ISTs in QWs is easily scalable throughout the infrared spectrum and occurs on a single resonator level involving only a small number of electrons [21]. Previous papers using other subwavelength geometries that include metallic backplanes have shown strong coupling at the single resonator level and/or a small number of carriers involved in the process [22–24]. We remark that such a backplane is not required to achieve subwavelength volumes as demonstrated recently in [21] or in this paper. This characteristic makes our MSs promising for the development of voltage-controlled tunable optical filters or modulators [25,26].

Strongly coupled systems using ISTs have been treated quantum mechanically [7,27,28]. Moreover, it has been shown that different resonator geometries may lead to different Rabi splittings [29], although an explanation of this phenomenon has not yet been provided. In this paper, we observe instead that the near fields responsible for the strong coupling can be simply and accurately described by the near fields of electrostatic dipoles, an approach not considered before. Our analysis addresses and explains phenomenologically the Rabi splitting dependence on the resonator geometry. This allows us to develop a closed-form expression for the MS resonator's capacitance that explicitly shows the strong-coupling contribution. From this, we develop an equivalent circuit network model that qualitatively and quantitatively describes the strong coupling processes.

We show that for the case of a flat MS made of dogbone resonators presented in Fig. 1(b), the results of the circuit network model are in good agreement with both full-wave simulations and experimental measurements. Hence, our network represents a low-order pole-zero polynomial expansion of the electromagnetic coupling between the MS resonance and

*Corresponding authors: sncampi@sandia.gov; f.capolino@uci.edu

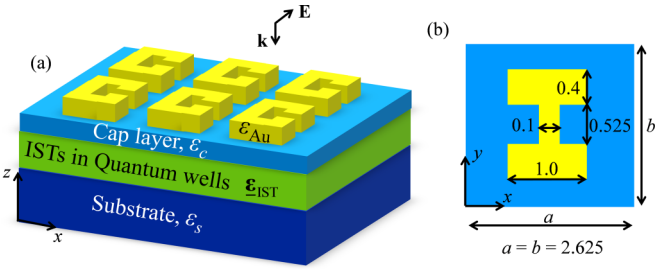

FIG. 1. (Color online) (a) 3D view of a MS made of split ring resonators (SRRs) on top of a multilayered substrate comprising QWs for strong coupling purposes (dimensions are not to scale). The normal plane wave illumination, with the electric field along y, is explicitly indicated. (b) Top view of the unit cell of a MS made of dogbone resonators. Dimensions in micrometers for the spatial scaling factor 1.0 are indicated (when the scaling factor is varied, all marked dimensions are scaled accordingly).

the ISTs. Next, we use the circuit network model to analyze strong coupling for three resonator geometries and observe that the magnitude of the Rabi splitting can be increased by increasing the MS resonators' capacitance. This capacitance can be understood either as one coefficient of the polynomial expansion of the coupling or as the physical capacitance of the quasistatic model developed next.

II. ELECTRODYNAMIC MODEL FOR FIELD-MATTER INTERACTION

Consider the structure in Fig. 1, where a MS of gold resonators (100 nm thick) is placed on top of a multilayered substrate comprising an $Al_{.48}In_{.52}As$ cap layer (30 nm thick) with relative permittivity $\varepsilon_c = 10.23$, a slab containing 20 repeat units of an $In_{.53}Ga_{.47}As/Al_{.48}In_{.52}As$ heterostructure (12.5/20 nm) supporting ISTs at a frequency of ~24.2 THz, and an InP substrate with $\varepsilon_s = 9.3$. The gold permittivity ε_{Au} is described using a Drude model [30] with parameters extracted from spectral ellipsometry measurements of a thin, 100-nm gold film, which yield a plasma angular frequency of $2\pi \times 2060 \times 10^{12}$ rad/s and a damping rate of $2\pi \times 10.9 \times 10^{12}$ rad/s. The ISTs are represented by anisotropic Lorentzian oscillators matched to experimental data, whose (relative) dielectric tensor is given as $\underline{\boldsymbol{\varepsilon}}_{IST} = \varepsilon_t(\hat{\mathbf{x}}\hat{\mathbf{x}} + \hat{\mathbf{y}}\hat{\mathbf{y}}) + \varepsilon_z\hat{\mathbf{z}}\hat{\mathbf{z}}$ [20,31,32], with $\varepsilon_t = 10.97$ and

$$\varepsilon_z = \varepsilon_t + \frac{f_z\omega_0^2}{\omega_0^2 - \omega^2 - 2i\omega\gamma} \tag{1}$$

where $\omega_0 = 2\pi \times 24.2 \times 10^{12}$ rad/s is the IST angular frequency, $\gamma = 2\pi \times 10^{12}$ rad/s represents the IST damping rate, and $f_z = 1.2$ is proportional to the IST oscillator strength, the doping density, and the intersubband matrix elements as described in [32]. (The monochromatic time harmonic convention $\exp(-i\omega t)$, used here and throughout the paper, is suppressed hereafter.)

Equation (1), together with the tensor $\underline{\boldsymbol{\varepsilon}}_{IST}$, reveals the selection rule for optical excitation of ISTs: only light polarized along the QWs' growth direction (here the z direction) can promote electrons between different subbands.

For a MS array with sufficiently subwavelength elements (Fig. 1) illuminated at normal incidence, the propagating incident, reflected, and transmitted waves do not contain z-polarized fields. However, substantial z-polarized electric fields are generated in the near field of the resonators within the array (see the appendix for more details). Due to the subwavelength dimensions of the MS resonators, the electric and magnetic near fields exhibit quasistatic behavior and hence are decoupled. Furthermore, because the electric near field of a dynamic dipole is equal to the field of a *static* dipole [33], we model each resonator as a distributed set of electrostatic charges to capture the contribution of the z-polarized fields of the MS subwavelength resonators. Hence, to begin, we consider the *electrostatic* problem of a single dipole located on the free space side and at a short distance from the interface between the free space and an anisotropic material with $\underline{\boldsymbol{\varepsilon}}_{IST}$ (see the appendix for more details). Following the steps outlined in [34,35], we estimate the static electric potential ϕ_e of the single dipole at any location in space. Assuming that the charges composing the single dipole are distributed over a tiny spherical surface with a radius much smaller than the charge separation, we obtain an approximate formula for the capacitance associated to such a dipole located close to the interface. Using the superposition of effects, summing over the distributed set of charges on the flat resonator allows us to obtain an expression for the total capacitance C of the resonator:

$$C = \frac{\sqrt{\varepsilon_t\varepsilon_z} + 1}{\varepsilon_t + 1} C_{ms} = C_{ms} + C_{eq}^{IST} = \xi C_{ms} \tag{2}$$

where C_{ms} is the MS resonator's capacitance per unit cell when no QWs are considered (i.e., $\varepsilon_z = \varepsilon_t$), $C_{eq}^{IST} = C_{ms}(\sqrt{\varepsilon_t\varepsilon_z} - \varepsilon_t)/(\varepsilon_t + 1)$ is the excess capacitance representing the strong coupling to the ISTs, and $\xi = (\sqrt{\varepsilon_t\varepsilon_z} + 1)/(\varepsilon_t + 1)$ is a coupling coefficient. Strictly speaking, ξ takes into account the perturbation of the electric field lines of the capacitor due to the presence of the ISTs in QWs with an anisotropic, frequency-dependent dielectric constant ε_z in Eq. (1). However, since the parameter ξ is introduced only in presence of QWs, it can also be understood as a coupling coefficient. We do not need to know the exact distribution of point charges in the MS since C_{ms} will be determined using the method described below. Nonetheless, the linear nature of the sums required for the calculation of C_{ms} and the establishment of an excess capacitance show that this method is general for any subwavelength resonator shape.

Circuit network theory is a common way to model metamaterial properties [36–42]. Equation (2) and the structure depicted in Fig. 1 allow for the construction of the equivalent circuit network model shown in Fig. 2, which embodies the physical processes of the bare flat MS, as well as the strong coupling to the QWs. The substrate branch (light blue dashed contour) consists of a resistor R_s that models the wave impedance of the dielectric layers below the MS. The MS is modeled via a resistance, inductance, and capacitance resonant circuit [37] (brown dashed contour) to capture the MS resonant features (i.e., the "cavity" resonance). The coupling to the ISTs in QWs is represented by the complex-valued equivalent excess capacitor C_{eq}^{IST}, which is arranged in parallel (green dashed contour) with the MS resonators' capacitance C_{ms}

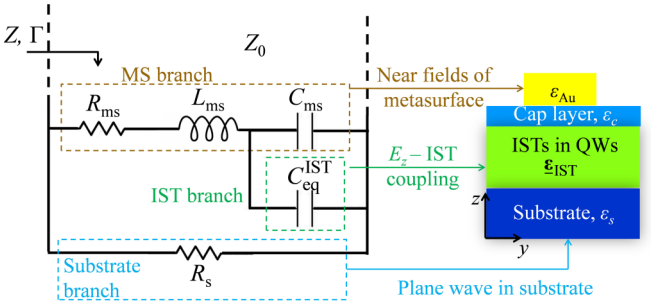

FIG. 2. (Color online) Circuit network model with MS impedance Z_{ms}, composed by R_{ms}, L_{ms}, and C_{ms}, and the equivalent capacitor C_{eq}^{IST}. The correlation of each circuit element to the real structure is marked by the dashed contours.

according to Eq. (2). Therefore, when the resonators reside on an isotropic substrate (i.e., no QWs), $\varepsilon_z = \varepsilon_t$, $C_{eq}^{IST} = 0$, and the total capacitance is $C = C_{ms}$. When instead we consider the flat resonators on top of the QWs, the total capacitance is $C = C_{ms} + C_{eq}^{IST} = \xi C_{ms}$, as in Eq. (2). From the above equation, we can estimate the coupling coefficient based on this quasistatic approximation as $\xi = (\sqrt{\varepsilon_t \varepsilon_z} + 1)/(\varepsilon_t + 1)$, which notably, as a first approximation, depends not on the MS geometry but only on the QW design.

To obtain the circuit parameters, a full-wave simulation (using a commercial frequency-domain, finite-element simulator [43]) of a MS without QWs is performed to determine the magnitude and phase of the plane wave reflection coefficient Γ under normal incidence illumination with an electric field polarized along y (we refer the phase to the top metal surface). We then use a commercial circuit simulator [44] to match the simulated Γ to the circuit reflection coefficient $\Gamma = (Z - Z_0)/(Z + Z_0)$, with $Z_0 = 377\Omega$ (illumination is from free space) and Z the input impedance of the circuit in Fig. 2, evaluated just above the MS. This matching procedure in the frequency band 15–40 THz leads to the frequency-independent circuit parameters R_s, R_{ms}, L_{ms}, and C_{ms}. The value of C_{eq}^{IST} is then simply obtained using Eq. (2)—*no further fitting is performed*. The circuit parameters for the dogbone resonator shown in Fig. 1(b) are given in Table I.

III. TOTAL ELECTRIC FIELD ENERGY EXCESS

To test the accuracy of our circuit model, we compare the energy and spectral properties obtained from the model with both full-wave simulations and experimental results. We

TABLE I. Rabi splitting from full-wave simulations and circuit parameter values in Fig. 2 for the three resonator shapes in Fig. 5 without QWs. We consider a scaling factor of 1.0 for the dogbone resonator and the circular SRR, and of 0.9 for the Jerusalem cross resonator.

Resonator	$\Omega_R/(2\pi)$ (THz)	C_{ms} (aF)	L_{ms} (pH)	R_{ms} (Ω)	R_s (Ω)
Circular SRR	2.1	8.7	4.6	51.8	111.7
Jerusalem cross	2.6	14.6	3.2	17.6	101.9
Dogbone	2.9	16.7	2.6	34.2	117.4

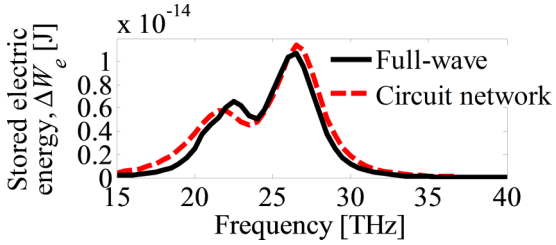

FIG. 3. (Color online) Stored electric energy ΔW_e per unit cell computed by full-wave simulations (solid black) and circuit network model (red dashed) for the dogbone resonator case in Fig. 1(b).

first consider the electric energy. In a medium characterized by a dispersive, absorptive permittivity tensor $\underline{\boldsymbol{\varepsilon}}_{IST}$, the time-averaged electric energy W_e contained within the unit cell volume V is evaluated as [45–47]

$$W_e = \int_V \left[\frac{1}{4}\varepsilon_0 \varepsilon_t |\mathbf{E}_t|^2 + \frac{1}{4}\varepsilon_0 \left(\varepsilon_z' + \frac{2\omega\varepsilon_z''}{2\gamma}\right)|E_z|^2\right] dV, \quad (3)$$

where $\varepsilon_z = \varepsilon_z' + i\varepsilon_z''$ and $\mathbf{E}_t$ and E_z are the transverse and longitudinal components, respectively, of the electric field generated by a (monochromatic) normal plane wave, with incident power $P = 1$ W per unit cell with area $A = ab$. Using the full-wave simulator, we perform the volumetric field integral over V representing the various regions of space in the simulation setup of Fig. 1, as described next. We evaluate energies in two situations: with and without QWs. Then, we estimate the amount of energy excess ΔW_e (shown as the black curve in Fig. 3) due to the presence of the Lorentzian IST resonance in the QWs as

$$\Delta W_e = W_e^{QW} - W_e^{\text{no QW}}, \quad (4)$$

where W_e^{QW} and $W_e^{\text{no QW}}$ are the total electric energies in the simulation with and without QWs, respectively. The term W_e^{QW} is computed by expanding the domain of integration into subdomains as

$$W_e^{QW} = \frac{1}{4}\varepsilon_0 \left(\varepsilon_z' + \frac{2\omega\varepsilon_z''}{2\gamma}\right)\int_{V_{QW}} |E_z^{QW}|^2 dV + \frac{1}{4}\varepsilon_0 \varepsilon_t \int_{V_{QW}} |\mathbf{E}_t^{QW}|^2 dV + \sum_i \frac{1}{4}\varepsilon_0 \varepsilon_i \int_{V_i} |\mathbf{E}^{QW}|^2 dV, \quad (5)$$

where the first two terms refer to the QW region in the unit cell and, in the last term, $i = \{\text{vacuum (200 nm), cap layer}\}$ represents the two volumetric regions outside the QWs in the unit cell. As a first approximation we include only a narrow portion (200-nm thickness) of the vacuum region because we only account for the near-field energy close to the resonators; likewise, we do not include the InP substrate because near fields decay rapidly within the QWs. The permittivity ε_z is dispersive in the QWs due to the ISTs; therefore, the energy must be calculated accordingly. The energy term $W_e^{\text{no QW}}$, in the absence of the QWs (and thus without ISTs), is instead computed as

$$W_e^{\text{no QW}} = \sum_j \frac{1}{4}\varepsilon_0 \varepsilon_j \int_{V_j} |\mathbf{E}^{\text{no QW}}|^2 dV, \quad (6)$$

with $j = \{\text{vacuum (200 nm), cap layer, isotropic QW layer}\}$, where the permittivity is nondispersive in all three volumetric regions. Approximations to the volumetric regions mentioned in regards to Eq. (5) are also applied to Eq. (6). These energies are computed numerically using total fields (i.e., including both plane wave and reactive components) obtained from full-wave simulation for both the absence and the presence of the QWs, properly dividing the integration regions and polarizations and considering the IST-induced frequency dispersion in the QWs. Close to the resonators (i.e., in the near field), the total field is, as a first approximation, dominated by the reactive components.

We now show that ΔW_e per unit cell can also be determined using the circuit model and compare it to the full-wave result. We can evaluate the magnitude of the driving (incident) electric field as $E_0 = \sqrt{2Z_0 P/A}$. The total transverse electric field at the input impedance terminals is then given by $\mathbf{E}_t = E_0(1+\Gamma)\hat{\mathbf{y}}$. The term W_e^{QW} is then computed, assuming an incident traveling voltage wave of $V_{\text{inc}} = E_0 b$, as

$$W_e^{\text{QW}} = \frac{1}{4}\left(C' + \frac{2\omega C''}{2\gamma}\right)\left|V_C^{\text{QW}}\right|^2, \tag{7}$$

where V_C^{QW} (evaluated as shown in the appendix) is the voltage acting on the total capacitor $C = C' + iC''$ given by Eq. (2). In Eq. (7), we have applied the same dispersive condition as in Eq. (3) in the framework of circuit theory [48], assuming a damping rate as in Eq. (1). The term $W_e^{\text{no QW}}$ is instead computed simply as

$$W_e^{\text{no QW}} = \tfrac{1}{4} C_{\text{ms}} \left|V_C^{\text{no QW}}\right|^2 \tag{8}$$

where $V_C^{\text{no QW}}$ is the voltage acting on the MS resonators' capacitor C_{ms} (evaluated as shown in the appendix). The energy difference due to the QWs obtained using this procedure is shown as the red dashed curve in Fig. 3. The agreement between the energy ΔW_e evaluated via full-wave simulations and that evaluated via circuit network theory shown is quite remarkable, given that the circuit network model is based on a quasistatic approximation and the coupling coefficient ξ in closed form, as in Eq. (2), and hence is extremely simple. If instead of using Eq. (2) we evaluate $C_{\text{eq}}^{\text{IST}}$ via a second fitting procedure, using the circuit simulator similar to what was done for C_{ms} but this time using full-wave data in the presence of QWs, the agreement for the peaks' locations would be further improved, validating the circuit topology in Fig. 2; however, our point is that even the simple formula in Eq. (2), with coupling coefficient ξ determined analytically, provides a good explanation.

IV. SPECTRAL REFLECTIVITY

Figure 4(a) shows the $|\Gamma|^2$ reflectivity maps obtained from full-wave simulations of the MS of dogbone resonators on top of QWs as a function of the bare cavity resonance, controlled by scaling the MS geometry. To generate this map, we simulated a set of MSs for which all spatial dimensions of the MS of dogbone resonators are scaled by a common scaling factor that varied between 0.7 and 1.2 [relative to the dimensions shown in Fig. 1(b)]. For each scaling factor, we performed a full-wave simulation of the MS without the QWs to determine the bare cavity resonance frequency as the location of maximum reflectivity. Next, we performed simulations including the QWs and plotted the obtained reflectivity spectra versus the bare cavity frequency. Figure 4(b) shows the corresponding maps obtained from the circuit model. For each scaling factor used in Fig. 4(a), we use the full-wave simulation result (without the QWs) to obtain the circuit parameters R_s, R_{ms}, L_{ms}, and C_{ms}. We then use Eq. (2) to calculate $C_{\text{eq}}^{\text{IST}}$, which is then inserted in the circuit model to obtain the reflectivity spectra. Finally, Fig. 4(c) shows the experimentally measured reflectivity spectra for a set of MSs with the same scaling factors [21]. The splitting around 24 THz is clearly visible in the experiment, as well as in the simulations. In addition, extremely good agreement between the circuit model and the full-wave simulation is observed. The small reflectivity magnitude mismatch in the experimental reflectivity with respect to other results is attributed to fabrication imperfections. The results in Fig. 4, together with those in Fig. 3, show that Eq. (2) is correct and confirm the

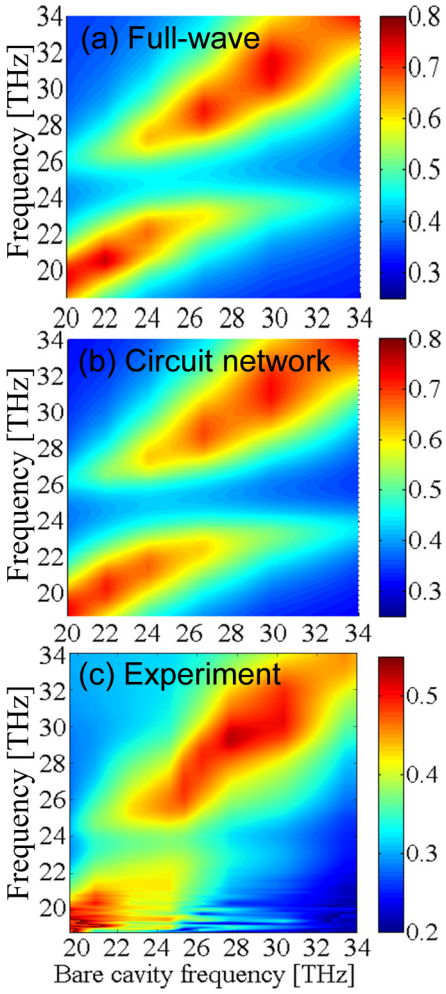

FIG. 4. (Color online) Maps of reflectivity $|\Gamma|^2$ from (a) full-wave simulation, (b) circuit network model, and (c) experimental setup for the dogbone structure in Fig. 1(b) with QWs. Only the values relative to bare cavity frequencies pertaining to scaling factors 0.7, 0.8, 0.9, 1.0, 1.1, and 1.2 were used. Continuous plots are shown for better visibility.

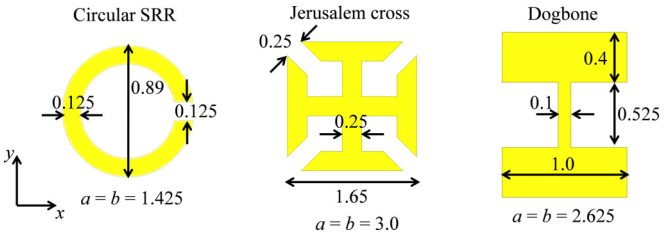

FIG. 5. (Color online) Three resonator structures, along with dimensions (in micrometers) for a scaling factor of 1.0.

validity of the circuit model introduced in Fig. 2. In turn, this implies that the electrostatic near fields of dipoles can be used to accurately describe the strong coupling processes, a result that may not be as straightforward in complex systems as the one analyzed here. To our knowledge, such an approach has never been described before.

V. PARAMETERS CONTROLLING THE COUPLING STRENGTH

It follows from Eq. (2) that only two parameters affect strong coupling: the capacitance C_{ms} and the coupling coefficient ξ. The coupling coefficient ξ is the only parameter that contains the Lorentzian dispersion in ISTs through the quantity $\sqrt{\varepsilon_t \varepsilon_z}$, but it does not contain information on the MS element shape, further stressing the elegance and simplicity of the proposed model. More efficient ISTs (i.e., stronger anisotropy, and thus larger ξ) might lead to larger splitting. For example, in our QW structure, the optically active transition happens between the ground state and the first excited state. A larger oscillator strength, and hence larger Rabi splitting, can be achieved through the use of transitions between higher states inside the same QW, for example as demonstrated in [18]. When comparing the performance of different resonator geometries using the same QWs, ξ will be unchanged and the magnitude of the coupling will only change if C_{ms} changes. Other MS circuit parameters will, in principle, also affect the spectral properties, because they contribute to reflection magnitude and resonance quality factor.

To elucidate the effect of the MS elements on strong coupling, we consider the three MSs based on the three resonator geometries shown in Fig. 5 (the dimensions of structures for scaling factor 1.0 are indicated therein): (1) circular split ring resonator (SRR); (2) Jerusalem cross; and (3) dogbone. The three MSs are on top of the same QWs described by $\underline{\boldsymbol{\varepsilon}}_{\mathrm{IST}}$. For each resonator type, we perform both full-wave and circuit model simulations over a range of scaling factors to map out the polariton branches, corresponding to the locations of two reflectivity maxima. The magnitude and phase of the reflection coefficient Γ for the three resonator geometries scaled to resonate with the ISTs are shown in Fig. 6. The top row of Fig. 6 shows the situation without QWs. A single resonance is observed for the three geometries, and in the vicinity of this resonance, the circuit model results (dashed curves) are in good agreement with full-wave results (solid curves). This result further shows that our fitting procedure recovers circuit parameters that accurately reproduce the resonant features of the MS when $C_{\mathrm{eq}}^{\mathrm{IST}} = 0$. Inserting $C_{\mathrm{eq}}^{\mathrm{IST}}$, obtained from Eq. (2), in the circuit model corresponds to the cases where QWs are present and leads to a splitting of the primary resonance, as is shown in the bottom row of Fig. 6. Again, good agreement between the circuit model and the

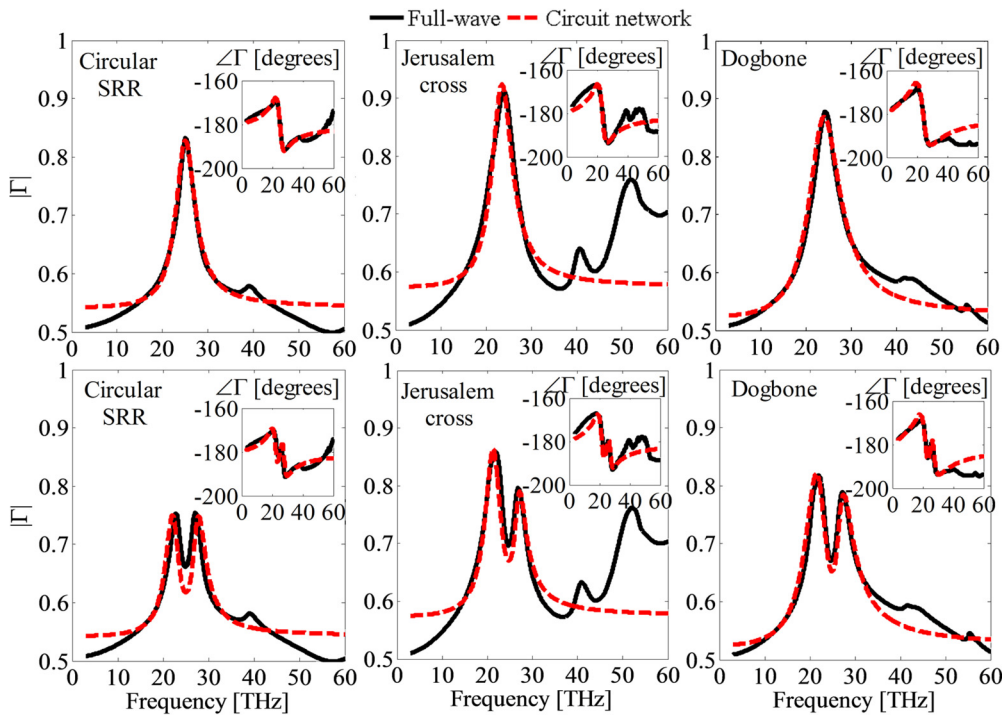

FIG. 6. (Color online) Magnitude and (unwrapped) phase of Γ from full-wave simulation (black solid) and circuit network model (red dashed) for the three structures in Fig. 5 without QWs (top row) and with QWs (bottom row). We consider a scaling factor of 1.0 for the dogbone resonator and the circular SRR, and of 0.9 for the Jerusalem cross resonator.

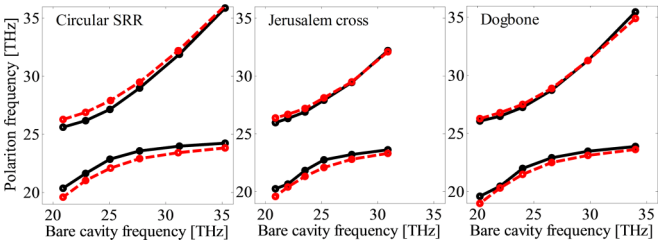

FIG. 7. (Color online) Plot of the two polariton branches versus the bare cavity frequency for the three resonator structures in Fig. 5 obtained from full-wave simulation (black solid) and circuit network theory (red dashed).

full-wave results is observed in the vicinity of the resonances. We recall that circuit parameters are retrieved considering the frequency range 15–40 THz and that if one also desires to match other frequencies, more complicated circuit branches will be necessary.

Figure 7 shows the two polariton branches as a function of the bare cavity frequency (controlled by the scaling factor) for the three resonators obtained using the circuit model and full-wave simulation. Excellent agreement with the full-wave results is obtained. These plots nicely show the splitting due to strong coupling, and through the use of Eq. (6) in [8], we are able to estimate the Rabi splitting Ω_R, which is reported in Table I. Table I also lists the circuit parameters R_s, $R_{\rm ms}$, $L_{\rm ms}$, and $C_{\rm ms}$ for each resonator geometry for the scaling factors that lead to nearly coincident MS and IST resonant frequencies. Specifically, these parameter correspond to the dogbone resonator and the circular SRR with a scaling of 1.0 and to the Jerusalem cross resonator with a scaling of 0.9. In the parameter retrieval, we have allowed $R_{\rm s}$ to slightly change for the different structures because higher-order transverse-magnetic-polarized modes may propagate into the substrate for the considered unit cell sizes and thus contribute to extra losses in the structure.

Importantly, we see from Table I that the capacitance values of the dogbone and Jerusalem cross resonators are similar in magnitude, leading to similar Rabi splittings. In contrast, the capacitance of the circular SRR is smaller, causing the narrower splitting observed in the full-wave result in the bottom row of Fig. 6 and in Fig. 7. This confirms the prediction made earlier that the splitting only depends on the value of $C_{\rm ms}$, assuming the coupling coefficient ξ does not change for the three cases. To confirm this observation, we redesigned the circular SRR with wider traces to increase its capacitance (diameter of 1.15 μm and traces of 0.35 μm for scaling factor 1.0, exhibiting $C_{\rm ms} \approx 13.7$ aF). With such a resonator, we get the expected larger Rabi splitting of $\Omega_R/(2\pi) \approx 2.4$ THz. Based upon our theory, we believe that the microcavity designs featuring metallic backplanes, such as the ones presented in [49,50], are good choices to enhance light-matter coupling, since they should be characterized by a large capacitance. However, to verify this concept, the current circuit model would need to be updated to account for the backplane.

We have seen that the Rabi splitting directly depends on the capacitance $C_{\rm ms}$ and thus on the resonator geometric parameters. For isolated SRRs without substrate, the capacitance can be expressed as [51] $C_{\rm SRR} = C_{\rm gap} + C_{\rm surf}$, with $C_{\rm gap} = \varepsilon_0 hw/g + \varepsilon_0 (h + w + g)$ (which comprises the parallel-plate capacitor formed by the gap and a correcting term due to the fringing fields) and $C_{\rm surf} = [2\varepsilon_0(h + w)\log(4R/g)]/\pi$ as the surface capacitance, where h is the SRR thickness, w is the SRR trace width, g is the SRR gap, and R is the SRR inner radius. Using such formulas for the two SRR geometries analyzed above, we obtain $C_{\rm SRR} \cong 7$ aF and $\cong$12.6 aF, respectively, showing the same order of magnitude as reported above for the two MSs. More accurate formulas would require us to account for the substrate. However, similar trends with geometric parameters are expected.

VI. CONCLUSION

We have reported an equivalent electrodynamic model for strong coupling between a MS and the ISTs in QWs by resorting to an equivalent circuit network theory and the electrostatic near fields of the flat MS dipoles. Such a model qualitatively and quantitatively explains the energy stored near the MS and the energy exchanged between the MS and the ISTs in QWs. It is also able to recover the reflection and transmission spectral properties of systems where electromagnetic fields and ISTs are strongly coupled. We have adopted this model at midinfrared frequencies, but our findings will apply in any given wavelength range. Despite the 3D (volumetric) nature of the light-matter coupling, we observed that the strong coupling mechanism is governed mainly by only two parameters: the coupling parameter ξ, which depends on the QW design and not on the MS geometry, and the MS resonator's capacitance $C_{\rm ms}$ in the absence of QWs. Although the use of the electrostatic fields of a dipole to describe the strong coupling process may at first seem surprising, its validity is based on two main observations. First, the QWs interact only with z-polarized electric fields. Due to the subwavelength period of the array, the propagating transmitted and reflected electric fields contain no z component. Thus, z-polarized fields occur only in the quasistatic (i.e., near-field) zone of the MS resonators and are well described by electrostatic dipolar fields. Second, near-field interactions among resonators in the MS are negligible due to the rapid decay of the fields. Through the use of this parameterization, we have demonstrated that the Rabi splitting increases with the capacitance $C_{\rm ms}$, thereby providing a phenomenological explanation of why different Rabi splittings have been observed with different resonator shapes. The results reported in this paper provide us with a pathway to increase the Rabi splitting by (1) optimizing the MS by increasing the resonators' capacitance and (2) optimizing the QW design (e.g., by increasing the oscillator strength). Such optimization may enable us to go beyond strong coupling regime by using planar MSs coupled to ISTs in QWs at infrared frequencies.

ACKNOWLEDGMENTS

This work was performed, in part, at the Center for Integrated Nanotechnologies, a U.S. Department of Energy, Office of Basic Energy Sciences, user facility. Portions of this work were supported by the Laboratory Directed Research and Development program at Sandia National Laboratories. Sandia National Laboratories is a multiprogram laboratory managed and operated by Sandia Corporation, a wholly owned subsidiary of Lockheed Martin Corporation, for the U.S.

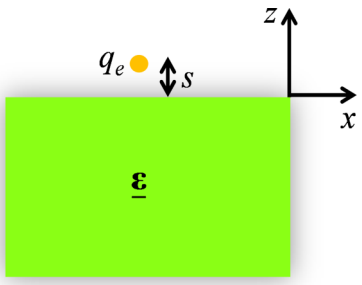

FIG. 8. (Color online) Point charge (in the free space region) located near the interface between an isotropic and a uniaxial anisotropic material.

Department of Energy's National Nuclear Security Administration under Contract No. DE-AC04-94AL85000. S.C. and F.C. thank Ansys Inc. and AWR Corporation for providing the High Frequency Structure Simulator and Microwave Office, respectively, which were instrumental in this paper.

APPENDIX

1. Steps to achieve Eq. (2)

Consider a uniaxial anisotropic material with a (relative) dielectric tensor

$$\underline{\boldsymbol{\varepsilon}} = \varepsilon_t\,(\hat{\mathbf{x}}\hat{\mathbf{x}} + \hat{\mathbf{y}}\hat{\mathbf{y}}) + \varepsilon_z \hat{\mathbf{z}}\hat{\mathbf{z}}. \tag{A1}$$

The displacement field is expressed as $\mathbf{D} = \underline{\boldsymbol{\varepsilon}} \cdot \mathbf{E}$. We also know that the equation $\nabla \cdot \mathbf{D} = \rho_e$ has to be satisfied, where ρ_e is the electric charge density. Limiting the analysis to electrostatic fields, because the structures used in the MS are subwavelength, the electric field near the MS resonators is well approximated by

$$\mathbf{E} = -\nabla \phi_e \tag{A2}$$

where ϕ_e is the scalar electric potential generated by the charge density ρ_e accumulated at the ends of the dogbone shape in Fig. 1(b), for example.

Consider now the scenario of a point charge q_e (thus $\rho_e = q_e \delta(\mathbf{r} - \mathbf{r}_e)$, with $\mathbf{r}_e = s\hat{\mathbf{z}}$) located close to the interface between the free space and a uniaxial anisotropic material (the ISTs in QWs), as shown in Fig. 8, where the point charge is in the free space side at a distance s from the interface.

Following the steps in Refs. [34,35], the potential ϕ_e at a point (x,y,z) within free space is given by

$$\phi_e = \frac{q_e}{4\pi\varepsilon_0}\left[\frac{1}{R_-} - \frac{\frac{\sqrt{\varepsilon_t\varepsilon_z}-1}{\sqrt{\varepsilon_t\varepsilon_z}+1}}{R_+}\right] \tag{A3}$$

where $R_\pm = \sqrt{x^2 + y^2 + (z \pm s)^2}$ represents the distance either from the charge or from its image, whereas within the anisotropic material, ϕ_e is

$$\phi_e = \frac{1}{4\pi\varepsilon_0}\frac{2q_e}{\sqrt{\varepsilon_t\varepsilon_z}+1}\frac{1}{\sqrt{x^2 + y^2 + \left(\sqrt{\frac{\varepsilon_t}{\varepsilon_z}}z - s\right)^2}} \tag{A4}$$

The potential is continuous across the interface at $z = 0$. Knowing Eqs. (A3) and (A4) for a single charge, we now consider a transverse dipole made of two displaced and opposite charges $\pm q_e$ with separation d located very close to the interface, i.e., $s = 0^+$. We further assume that the charges are uniformly distributed around small spherical surfaces with radius $r_c \ll d$ (so that we can consider it uniformly distributed). We can then estimate the capacitance associated with such a two-charge system as

$$C = \frac{q_e}{\phi_+ - \phi_-}, \tag{A5}$$

where $\phi_+ - \phi_-$ is the potential difference between the two charges and ϕ_+ and ϕ_- are the potentials at the surface of the positive and negative charge spherical distributions, respectively.

Using Eq. (A3), the potential at any observation point within free space is

$$\phi_e = \frac{q_e}{4\pi\varepsilon_0 r_1}\left[1 - \frac{\sqrt{\varepsilon_t\varepsilon_z}-1}{\sqrt{\varepsilon_t\varepsilon_z}+1}\right] - \frac{q_e}{4\pi\varepsilon_0 r_2}\left[1 - \frac{\sqrt{\varepsilon_t\varepsilon_z}-1}{\sqrt{\varepsilon_t\varepsilon_z}+1}\right] \tag{A6}$$

where r_1 and r_2 are the distances from the given observation point to the positive and negative charge positions, respectively. In particular, for the observation point at the surface location of the positive distributed charge, we have $r_1 = r_c$ and $r_2 \approx d$ because $r_c \ll d$. Therefore, the potential ϕ_+ is given by

$$\phi_+ = \frac{q_e}{4\pi\varepsilon_0}\frac{2}{\sqrt{\varepsilon_t\varepsilon_z}+1}\left(\frac{1}{r_c} - \frac{1}{d}\right). \tag{A7}$$

Similarly, at the surface location of the negative distributed charge, we have $r_1 \approx d$ because $r_c \ll d$ and $r_2 = r_c$, so the potential ϕ_- is given by

$$\phi_- = \frac{q_e}{4\pi\varepsilon_0}\frac{2}{\sqrt{\varepsilon_t\varepsilon_z}+1}\left(\frac{1}{d} - \frac{1}{r_c}\right). \tag{A8}$$

Thus, the potential difference is equal to

$$\phi_+ - \phi_- = \frac{q_e}{4\pi\varepsilon_0}\frac{4}{\sqrt{\varepsilon_t\varepsilon_z}+1}\left(\frac{1}{r_c} - \frac{1}{d}\right). \tag{A9}$$

Therefore, we can obtain the formula for the capacitance, under the assumption $r_c \ll d$:

$$C = \pi\varepsilon_0 r_c(\sqrt{\varepsilon_t\varepsilon_z}+1). \tag{A10}$$

In this construction, the charge size r_c does not need to be known. (Any distribution can be used; however, this would result in different geometrical factors in Eq. (A10) instead of the factor r_c.) The capacitance associated with the same two-charge system on top of a fully isotropic material (i.e., when the anisotropic layer is replaced by an isotropic material with $\varepsilon_z = \varepsilon_t$) is $C_0 = \pi\varepsilon_0 r_c(\varepsilon_t + 1)$. (In free space, $\varepsilon_t = 1$ and $C_0 = 2\pi\varepsilon_0 r_c$ as the result in the literature for a two-charge system in free space [52–56].) Therefore, we can rewrite Eq. (A10) as

$$C = \frac{\sqrt{\varepsilon_t\varepsilon_z}+1}{\varepsilon_t+1}C_0 = \xi C_0 \tag{A11}$$

and most importantly, the ratio $C/C_0 = (\sqrt{\varepsilon_t\varepsilon_z}+1)/(\varepsilon_t+1)$ does not depend on the unknown size r_c of the charge distribution.

A flat resonator (like those in Figs. 1 and 5) is in general described by a distributed set of charge pairs, i.e.,

dipoles sharing the same potential difference under the static approximation. To determine the same functional dependence C/C_0 shown above for a set of charges, we assume that the charge distribution is flat; i.e., all charges are at the same distance from the substrate underneath. This in turn means that the effect of each pair of charges is accounted for by Eq. (A11) and that after applying the superposition of effects, Eq. (A11) can be generalized to Eq. (2) by substituting $C_{\rm ms}$ for C_0, which results from the summation over the resonator's distributed charge distributions. This is an approximate equation to model the complex system of a flat MS and the ISTs in QWs underneath. The use of Eq. (A11) provides us with the means for understanding which parameters affect the strong coupling processes and is found to be remarkably accurate for the analyzed flat MSs, also based on what is shown in the next section.

2. Comparison of electric fields under a MS made of dogbone resonators, calculated with electrostatic and full-wave models

We show that the field generated by a set of electrostatic charges placed on the paddles of a dogbone resonator, as in Fig. 9, recovers the electric field calculated via full-wave simulations, validating the quasistatic approximation used in the circuit model.

To do so, we perform two full-wave simulations of a MS made of dogbone resonators: (1) as in Fig. 1, where the anisotropic region has finite thickness, denoted as Full-wave 1, and (2) as in Fig. 8, where the anisotropic region has infinite thickness, denoted as Full-wave 2. In both simulations, the environment below the resonators starts at $z = 0$. We then apply the formalism reported in Eq. (A2) in the prior section at the IST resonance frequency of 24.2 THz and evaluate the electrostatic field generated by two sets of opposite charges uniformly distributed on the two paddles of the dogbone, as in Fig. 9 (we consider them to be at $z = s = 50$ nm, i.e., midway through the thickness of the dogbone resonator). The anisotropic region starts at $z = 0$.

We then show in Fig. 10 the magnitude of the electric field components (each component is normalized to its own maximum) in the x-y plane (cut at $z = -100$ nm for all simulation setups within the anisotropic region). The two full-wave simulations provide similar electric field patterns (the decay along the z direction is also similar but is not shown for brevity), so the approximation that assumes the anisotropic medium below the MS to be half space can be safely applied to determine the electric fields and thus the capacitance. In the presence of QWs, the strongest near-field component at resonance is the E_z component for all resonator shapes considered. This in turn shows that with QWs present, most of the electric energy is stored by E_z in the near fields of the resonators. This is precisely the field component required for the excitation of the ISTs according to the dipole selection rule. However, in the absence of QWs the strength of the E_z relative to the other field components depends upon the resonator shape. However, in the electrostatic case in Fig. 10, which provides field distributions in remarkable agreement, we are simulating an isolated unit cell, not a periodic set of dogbones. Therefore, coupling among MS unit cells is neglected in this simulation. Moreover, we are considering a uniformly distributed set of charges on the dogbone paddles, and this seems not to be exactly the case when looking at full-wave simulation results. Nonetheless, the result in Fig. 10 proves that the near-zone electric field generated by the dogbones can be predicted by a distribution of electric dipoles. As such, the electrostatic approximation adopted in part of this paper is valid. Finally, in the equivalent circuit model, the capacitors mainly store only electric energy, which is associated to the volumetric integrals integrating the strong energy density over the small volume above and below the MS elements. In particular, $C_{\rm eq}^{\rm IST}$ is defined assuming only E_z, and since this field component cannot propagate away from the MS, it is completely defined in the near field.

Though the circuit model uses capacitors to represent the MS-QW coupling, highlighting the E_z electric energy channel for the strong coupling, the circuit model in Fig. 2 could also be devised based on a simple pole-zero expansion in the polynomial approximation of the numerator and the denominator of the reflection coefficient Γ. Indeed, it is well known that certain polynomial expansions are associated with realizable (i.e., physical) passive circuit elements and that the polynomial coefficients can be expressed in terms of lumped elements values. Therefore, despite the use of a static approximation in this paper, such equivalent circuit models can be generalized to more complicated structures.

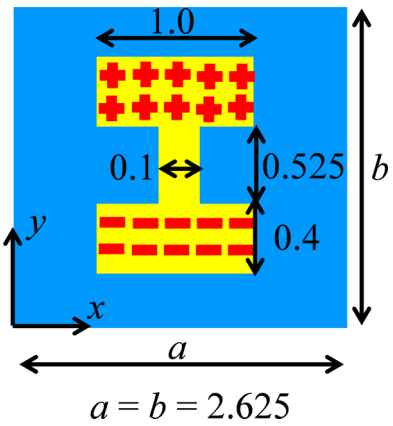

FIG. 9. (Color online) Sketch of the two sets of electrostatic positive and negative charges displaced on the paddles of a dogbone resonator (the charges are uniformly distributed). Dimensions in micrometers are reported.

3. Computation of $V_C^{\rm QW}$ and $V_C^{\rm no\,QW}$ in Eqs. (7) and (8)

We provide here the steps to compute the voltages $V_C^{\rm QW}$ and $V_C^{\rm no\,QW}$ across the capacitors, with and without QWs in the region below the MS, as required for the calculation of the energy ΔW_e via circuit network theory.

Given the circuit model in Fig. 2, and knowing the incident traveling voltage wave $V_{\rm inc} = E_0 b$, evaluated just above the MS layer, the total transverse voltage at the input impedance terminals accounts for the reflected wave as $V_t = E_0(1 + \Gamma)b$. The current flowing in the upper branch of the circuit network can be calculated as follows. Let us consider first the case without QWs (i.e., $C_{\rm eq}^{\rm IST} = 0$). In such a case, the current

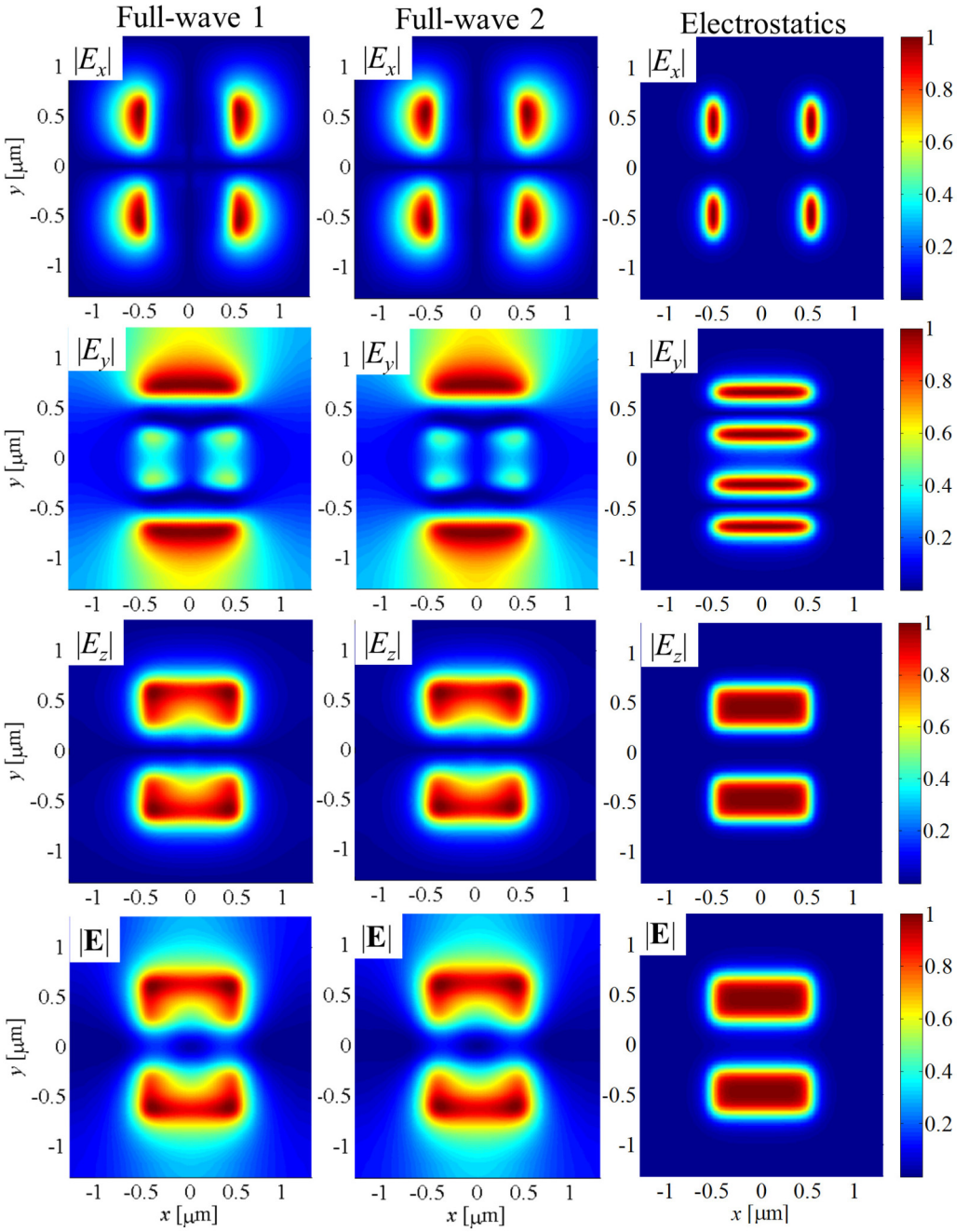

FIG. 10. (Color online) Magnitude of the electric field components in the x-y plane (cut at $z = -100$ nm for all simulation setups within the anisotropic region) in the case of a MS made of dogbone resonators. Comparison between electrostatic and full-wave solutions shows agreement. The difference between the two full-wave simulations is in the anisotropic region thickness, of finite extent for Full-wave 1 and infinite extent for Full-wave 2, as described in the text.

flowing in the MS branch is given by

$$I_{\rm ms} = \frac{V_t}{Z_{\rm ms}} = \frac{E_0(1+\Gamma)b}{R_{\rm ms} - i\omega L_{\rm ms} + i/(\omega C_{\rm ms})}. \tag{A12}$$

The voltage across the MS capacitor is then given by the generalized Ohm's law for impedances:

$$V_C^{\rm no\,QW} = \frac{i}{\omega C_{\rm ms}} I_{\rm ms}. \tag{A13}$$

In the presence of QWs, similar steps can be applied. In particular, assuming the two capacitors in parallel, $I_{\rm ms}$ is now given by

$$I_{\rm ms} = \frac{V_t}{Z'} = \frac{E_0(1+\Gamma)b}{R_{\rm ms} - i\omega L_{\rm ms} + i/\left[\omega\left(C_{\rm ms} + C_{\rm eq}^{\rm IST}\right)\right]}. \tag{A14}$$

The voltage across the IST capacitor is then given by

$$V_C^{\rm QW} = \frac{i}{\omega\left(C_{\rm ms} + C_{\rm eq}^{\rm IST}\right)} I_{\rm ms}. \tag{A15}$$

[1] V. G. Veselago, Sov. Phys. Usp. **10**, 509 (1968).
[2] R. A. Shelby, D. R. Smith, and S. Schultz, Science **292**, 77 (2001).
[3] J. B. Pendry, Phys. Rev. Lett. **85**, 3966 (2000).
[4] N. Fang, H. Lee, C. Sun, and X. Zhang, Science **308**, 534 (2005).
[5] J. C. Ginn, I. Brener, D. W. Peters, J. R. Wendt, J. O. Stevens, P. F. Hines, L. I. Basilio, L. K. Warne, J. F. Ihlefeld, P. G. Clem, and M. B. Sinclair, Phys. Rev. Lett. **108**, 097402 (2012).
[6] D. Schurig, J. J. Mock, B. J. Justice, S. A. Cummer, J. B. Pendry, A. F. Starr, and D. R. Smith, Science **314**, 977 (2006).
[7] S. De Liberato, C. Ciuti, and I. Carusotto, Phys. Rev. Lett. **98**, 103602 (2007).
[8] Y. Todorov, A. M. Andrews, R. Colombelli, S. De Liberato, C. Ciuti, P. Klang, G. Strasser, and C. Sirtori, Phys. Rev. Lett. **105**, 196402 (2010).
[9] J. P. Reithmaier, G. Sęk, A. Löffler, C. Hofmann, S. Kuhn, S. Reitzenstein, L. V. Keldysh, V. D. Kulakovskii, T. L. Reinecke, and A. Forchel, Nature **432**, 197 (2004).
[10] A. A. Anappara, A. Tredicucci, G. Biasiol, and L. Sorba, Appl. Phys. Lett. **87**, 051105 (2005).
[11] A. A. Anappara, A. Tredicucci, F. Beltram, G. Biasiol, and L. Sorba, Appl. Phys. Lett. **89**, 171109 (2006).
[12] G. Günter, A. A. Anappara, J. Hees, A. Sell, G. Biasiol, L. Sorba, S. De Liberato, C. Ciuti, A. Tredicucci, A. Leitenstorfer, and R. Huber, Nature **458**, 178 (2009).
[13] D. Englund, A. Majumdar, A. Faraon, M. Toishi, N. Stoltz, P. Petroff, and J. Vuckovic, Phys. Rev. Lett. **104**, 073904 (2010).
[14] S. Zanotto, G. Biasiol, R. Degl'Innocenti, L. Sorba, and A. Tredicucci, Appl. Phys. Lett. **97**, 231123 (2010).
[15] R. Huber, A. A. Anappara, G. Günter, A. Sell, S. De Liberato, C. Ciuti, G. Biasiol, L. Sorba, A. Tredicucci, and A. Leitenstorfer, J. Appl. Phys. **109**, 102418 (2011).
[16] M. Porer, J.-M. Ménard, A. Leitenstorfer, R. Huber, R. Degl'Innocenti, S. Zanotto, G. Biasiol, L. Sorba, and A. Tredicucci, Phys. Rev. B **85**, 081302(R) (2012).
[17] P. Jouy, A. Vasanelli, Y. Todorov, A. Delteil, G. Biasiol, L. Sorba, and C. Sirtori, Appl. Phys. Lett. **98**, 231114 (2011).
[18] A. Delteil, A. Vasanelli, Y. Todorov, C. Feuillet Palma, M. Renaudat St-Jean, G. Beaudoin, I. Sagnes, and C. Sirtori, Phys. Rev. Lett. **109**, 246808 (2012).
[19] G. Scalari, C. Maissen, D. Hagenmüller, S. De Liberato, C. Ciuti, C. Reichl, W. Wegscheider, D. Schuh, M. Beck, and J. Faist, J. Appl. Phys. **113**, 136510 (2013).
[20] D. Dietze, A. Benz, G. Strasser, K. Unterrainer, and J. Darmo, Optic. Express **19**, 13700 (2011).
[21] A. Benz, S. Campione, S. Liu, I. Montano, J. F. Klem, A. Allerman, J. R. Wendt, M. B. Sinclair, F. Capolino, and I. Brener, Nat. Comm. **4**, 2882 (2013).
[22] C. Feuillet-Palma, Y. Todorov, R. Steed, A. Vasanelli, G. Biasiol, L. Sorba, and C. Sirtori, Optic. Express **20**, 29121 (2012).
[23] C. Feuillet-Palma, Y. Todorov, A. Vasanelli, and C. Sirtori, Sci. Rep. **3**, 1361 (2013).
[24] A. Benz, S. Campione, S. Liu, I. Montano, J. F. Klem, M. B. Sinclair, F. Capolino, and I. Brener, Optic. Express **21**, 32572 (2013).
[25] A. Benz, I. Montano, J. F. Klem, and I. Brener, Appl. Phys. Lett. **103**, 263116 (2013).
[26] Y. C. Jun, J. Reno, T. Ribaudo, E. Shaner, J.-J. Greffet, S. Vassant, F. Marquier, M. Sinclair, and I. Brener, Nano Lett. **13**, 5391 (2013).
[27] C. Ciuti, G. Bastard, and I. Carusotto, Phys. Rev. B **72**, 115303 (2005).
[28] Y. Todorov and C. Sirtori, Phys. Rev. B **85**, 045304 (2012).
[29] C. Maissen, G. Scalari, F. Valmorra, C. Reichl, D. Schuh, W. Wegscheider, M. Beck, S. de Liberato, D. Hagenmüller, C. Ciuti, and J. Fais, Proc. SPIE **8623**, 86231M (2013).
[30] M. A. Ordal, L. L. Long, R. J. Bell, S. E. Bell, R. R. Bell, J. R. W. Alexander, and C. A. Ward, Appl. Opt. **22**, 1099 (1983).
[31] A. Gabbay and I. Brener, Optic. Express **20**, 6584 (2012).
[32] A. Gabbay, J. Reno, J. R. Wendt, A. Gin, M. C. Wanke, M. B. Sinclair, E. Shaner, and I. Brener, Appl. Phys. Lett. **98**, 203103 (2011).
[33] J. D. Jackson, *Classical Electrodynamics* (Wiley, New York, 1999).
[34] R. Saraei and J. Rashed-Mohassel, J. Electromagn. Waves Appl. **17**, 1075 (2003).
[35] E. J. Mele, Am. J. Phys. **69**, 557 (2001).
[36] S. Young Jun and K. Sarabandi, IEEE Antenn. Wireless Propag. Lett. **11**, 1366 (2012).
[37] F. Capolino, A. Vallecchi, and M. Albani, IEEE Trans. Antenn. Propag. **61**, 852 (2013).
[38] H. Chen, L. Ran, J. Huangfu, T. M. Grzegorczyk, and J. A. Kong, J. Appl. Phys. **100**, 024915 (2006).
[39] F. Bilotti, A. Toscano, L. Vegni, K. Aydin, K. B. Alici, and E. Ozbay, IEEE Trans. Microw. Theor. Tech. **55**, 2865 (2007).
[40] M. Garcia-Vigueras, F. Mesa, F. Medina, R. Rodriguez-Berral, and J. L. Gomez-Tornero, IEEE Trans. Antenn. Propag. **60**, 4637 (2012).
[41] Y. Nakata, T. Okada, T. Nakanishi, and M. Kitano, Phys. Status Solidi B **249**, 2293 (2012).
[42] E. Shamonina, V. A. Kalinin, K. H. Ringhofer, and L. Solymar, J. Appl. Phys. **92**, 6252 (2002).
[43] Ansys, High Frequency Structure Simulator (HFSS), http://ansys.com/ (2013).
[44] AWR, AWR Microwave Office, http://www.awrcorp.com (2013).
[45] R. Loudon, J. Appl. Phys. Gen. Phys. **3**, 233 (1970).
[46] R. Ruppin, Phys. Lett. A **299**, 309 (2002).
[47] F. D. Nunes, T. C. Vasconcelos, M. Bezerra, and J. Weiner, J. Opt. Soc. Am. B **28**, 1544 (2011).
[48] K. J. Webb and Shivanand, J. Opt. Soc. Am. B **27**, 1215 (2010).
[49] E. Strupiechonski, G. Xu, M. Brekenfeld, Y. Todorov, N. Isac, A. M. Andrews, P. Klang, C. Sirtori, G. Strasser, A. Degiron, and R. Colombelli, Appl. Phys. Lett. **100**, 131113 (2012).
[50] E. Strupiechonski, G. Xu, P. Cavalié, N. Isac, S. Dhillon, J. Tignon, G. Beaudoin, I. Sagnes, A. Degiron, and R. Colombelli, Phys. Rev. B **87**, 041408(R) (2013).
[51] O. Sydoruk, E. Tatartschuk, E. Shamonina, and L. Solymar, J. Appl. Phys. **105**, 014903 (2009).
[52] J. Lekner, J. Electrost. **69**, 11 (2011).
[53] A. Russell, Proc. R. Soc. A **97**, 160 (1920).
[54] A. Russell, Proc. Phys. Soc. Lond. **23**, 352 (1910).
[55] G. B. Jeffery, Proc. R. Soc. A **87**, 109 (1912).
[56] L. D. Landau and E. M. Lifshitz, *Electrodynamics of Continuous Media* (Pergamon, New York, 1984).